RSC Advances

PAPER

View Article Online
View Journal | View Issue

Cite this: *RSC Adv.*, 2026, **16**, 28352

Synthesis of nano-copper chelated hierarchical biocomposite from eggshell membrane hydrolysate for visible-light-driven dye degradation

Aqsa Anam, [a] Asif Ayub, [a] Haq Nawaz, [b] Muhammad Altaf Nazir, [a] Riyadh H. Alshammari,[c] Abdul Rauf,[a] Aziz ur Rehman[a] and Muhammad Arshad *[a]

Received 8th November 2025
Accepted 19th May 2026

DOI: 10.1039/d5ra08632a

rsc.li/rsc-advances

A green synthesis approach was adopted to synthesize a nano-copper chelated hierarchical biocomposite (nCu-CHB) from an eggshell membrane (ESM) protein hydrolysate. The structural features of the synthesized material were investigated through XRD, FTIR, and XPS, while its morphological features were investigated using SEM, EDX, and TEM. The surface area, thermal stability and optical properties were evaluated using BET, TGA, and UV-vis spectroscopy, respectively. The results demonstrated that nCu-CHB exhibits a porous and wrinkled morphology with uniformly distributed copper nanoparticles, ranging from 5–9 nm. The material showed a surface area of approximately 14.25 $m^2\ g^{-1}$ and an optical band gap of 2.0 eV. The eco-friendly biocomposite demonstrated excellent visible-light photocatalytic performance, achieving up to 98.09% degradation of methylene blue (MB) within 90 min at neutral pH. Kinetic studies indicated that the degradation behavior followed pseudo-first-order kinetics (k = 0.0432 min^{-1}, R^2 = 0.9975). This work presents a promising approach for developing multifunctional biocomposite materials from ESM hydrolysate for the eradication of hazardous pollutants from water.

1 Introduction

A significant amount of toxic contaminants, including heavy metals, organic dyes, antibiotics, and microbial pollutants, are continuously discharged into soils and aquatic systems due to rapid population growth and industrialization.[1] Among these, synthetic dyes are major contributors to industrial wastewater originating from leather, textile, paint, plastic, cosmetics, carpet, and paper industries.[2,3] Over 100 000 types of dyes (almost 7×10^5 tons) are manufactured annually worldwide, with approximately 10% being released from the textile and associated sectors.[4,5] Due to their complex aromatic structure and non-biodegradable nature, these dyes remain stable in water bodies, hinder light transmission, thereby disrupting photosynthesis and posing risks to ecological systems and human health.[6] Methylene blue (MB) is widely used for staining wool, silk, cotton, and for biological applications.[7] Several methodologies have been employed to remove toxic pollutants from wastewater, including adsorption,[8] ozonation,[9] biological treatment,[10] flocculation,[11] and coagulation.[12] However, these methods face several limitations including incomplete removal, secondary waste generation, complex process requirements and high operational costs.[13]

Advanced oxidation processes (AOPs) are widely recognized as efficient wastewater treatment techniques, as they enable the degradation of refractory organic compounds through highly oxidative reactions while producing minimal secondary pollution. Depending on the reaction conditions, AOPs include photocatalysis, Fenton and Fenton-like reactions, electrochemical oxidation and sonochemical oxidation. Among these, photocatalysis is widely regarded as an environmentally friendly approach as semiconductor catalysts under visible-light irradiation lead to the production of hydroxyl and superoxide radicals that effectively degrade organic contaminants.[14] Moreover, photocatalytic efficiency can be improved through band gap tuning, structural and morphological modification, improved charge separation and enhanced surface adsorption properties.[15]

Recently, biopolymer-based composite materials have attracted increasing attention as photocatalysts for the degradation of organic contaminants and have been utilized for the degradation of organic dyes into harmless by-products.[16–19] Biomaterials are biodegradable, have minimal adverse effects on living organisms and the environment, and are also considered sustainable alternatives to chemically synthesized materials. Surface functionalization of biopolymers significantly improves their mechanical properties and thermal stability.[20] The abundance of functional groups including amine ($-NH_2$), hydroxyl (–OH), carboxylate ($-COO^-$), and thiol (–

[a]*Institute of Chemistry, The Islamia University of Bahawalpur, Baghdad-ul-Jadeed Campus, Bahawalpur 63100, Pakistan. E-mail: muhammad.arshad@iub.edu.pk*
[b]*School of Chemistry and Chemical Engineering, Huaiyin Normal University, Huaiyin, 223300, Jiangsu, China*
[c]*Department of Chemistry, College of Science, King Saud University, Riyadh 11451, Saudi Arabia*

SH) groups, on biopolymers plays a key role in chelating with metal ions for chemical modification.[21] The chelated biocomposites have several environmental applications, including the photocatalytic degradation of dyes.[22,23]

Eggshell membrane (ESM), a collagen-rich biopolymer composed of protein fibers, possesses a high density of surface functional groups including carboxyl (–COOH), hydroxyl (–OH), and amine ($–NH_2$) groups, which provide excellent binding sites for metals ions for the fabrication of composites.[24] It is biodegradable, non-toxic, and abundantly available as food waste.[25] ESM has been widely utilized for energy storage, laser support, biosorbents, biotemplates, biosensors, and medical applications.[26] Several studies have reported the utilization of ESM for the removal of toxic pollutants such as nickel (Ni),[27] chromium (Cr),[28] nitrophenol,[29] methylene blue (MB),[30] Congo red,[31] and Reactive Red 120.[26] Pant *et al.* utilized carbonized ESM to fabricate CdS–TiO_2/CESM composite to induce synergistic effects of adsorption and photocatalysis. The synthesized CdS–TiO_2/CESM composite showed effective removal of MB.[32] In another study, Zhou *et al.* fabricated BiOCl/CESM composite for mineralization of Rhodamine B and *o*-nitrophenol.[33] Similarly, Wu *et al.* synthesized an ESM/Cu_2O catalyst to improve the photocatalytic activity, which reached 97% degradation efficiency with methylene blue as a target pollutant.[34] However, most of the previous reports primarily employed ESM as a physical support or template for pre-formed semiconductor materials, while systematic investigations on direct metal ion chelation with hydrolyzed ESM matrix and its influence on electron transfer behaviour remain limited.

Incorporating transition metals into biopolymers is an effective strategy to enhance photocatalytic performance.[35] Among them, copper nanoparticles have attracted considerable attention in dye degradation applications due to their high surface area, strong redox activity, and excellent electrical conductivity. Unlike noble metals including silver, gold, and palladium, copper offers significant advantages in terms of lower cost, wide availability, and practical scalability for large-scale environmental applications. Under visible light irradiation, copper nanoparticles exhibit localized surface plasmon resonance, which enhances light harvesting and enables the production of photoinduced charge carriers. These photo induced electrons and holes participate in redox reactions, producing reactive oxygen species such as superoxide and hydroxyl radicals, which are highly effective in decomposing dye molecules. Furthermore, copper demonstrates favorable adsorption capability and redox flexibility, enabling efficient catalytic performance in wastewater treatment.[36] The abundant functional groups of ESM provide coordination sites for Cu^{2+} ion, enabling chelation and electronic interaction within the biopolymeric matrix.[37] Therefore, copper incorporation into the ESM is expected to improve visible-light responsiveness and catalytic efficiency.

Based on the above discussion, a nano-copper chelated hierarchical biocomposite (nCu-CHB) was fabricated from ESM hydrolysate. The present work focuses on the direct incorporation of copper ions within a hydrolyzed biopolymeric matrix to modify its electronic structure and visible light responsiveness. The effect of Cu^{2+} incorporation on optical, structural, and thermal characteristics was systematically investigated to establish a structure–property relationship. A detailed investigation of MB degradation under visible-light irradiation was conducted, focusing on the role of several factors including catalyst amount, dye concentration, irradiation time, and pH, to clarify the role of Cu-biopolymer coordination in enhancing photocatalytic performance.

2 Materials and methods

2.1 Chemicals

Copper chloride dihydrate ($CuCl_2 \cdot 2H_2O \geq 99\%$), *p*-benzoquinone (*p*-BQ), ≥98%, isopropyl alcohol (IPA), ≥99.5%, ammonium oxalate (AO), ≥99%, silver nitrate ($AgNO_3 \geq 99\%$), sodium hydroxide (NaOH, ≥98%), and methylene blue ($C_{16}H_{18}ClN_3S$, ≥95%) were obtained from Sigma-Aldrich (Germany). Ethanol (C_2H_5OH, ≥99.9%) and hydrochloric acid (HCl, 37%) were purchased from Merck (Germany). All reagents of analytical-grade purity were used in this study and double-distilled (DD) water was utilized for all experimental procedures.

2.2 Collection of ESM

Raw hen eggshells were collected from a local market in Bahawalpur, Pakistan. The eggshell membranes were peeled off manually, rinsed with DD water to remove impurities, and subsequently dried at room temperature. The dried membranes were then cut into small pieces for subsequent synthesis of the composite.

2.3 Synthesis of copper chelated biocomposite

Copper chelated biocomposite was synthesized *via* the chemical precipitation method using ESM hydrolysate as a biopolymeric matrix (Scheme 1), following previously reported strategies.[34] Briefly, 10 g of ESM pieces were hydrolyzed in 250 mL of 1 M NaOH solution under continuous stirring at 80 °C until complete dissolution, yielding a homogeneous ESM hydrolysate rich in amino, carboxylate, and hydroxyl functional groups. The selected ESM amount was chosen to ensure sufficient availability of active functional groups for effective metal chelation while maintaining the processability of the hydrolysate. Subsequently, 50 mL of 1 M $CuCl_2 \cdot 2H_2O$ solution was slowly introduced dropwise under constant stirring. The Cu^{2+} concentration was selected based on preliminary trials and literature-reported metal biopolymer chelation systems, ensuring effective copper incorporation without excess salt usage or secondary-phase formation. The dark green precipitates were formed immediately upon addition of the salt solution, and the suspension was maintained under stirring for an additional 30 min to ensure complete reaction. The precipitates obtained were isolated, and thoroughly washed with deionized water several times followed by washing with ethanol. After each washing step, the product was separated through centrifugation at 4000 rpm and subsequently dried at 100 °C for 3 h. The obtained product was pulverized into fine powder for further characterization and photocatalytic applications.

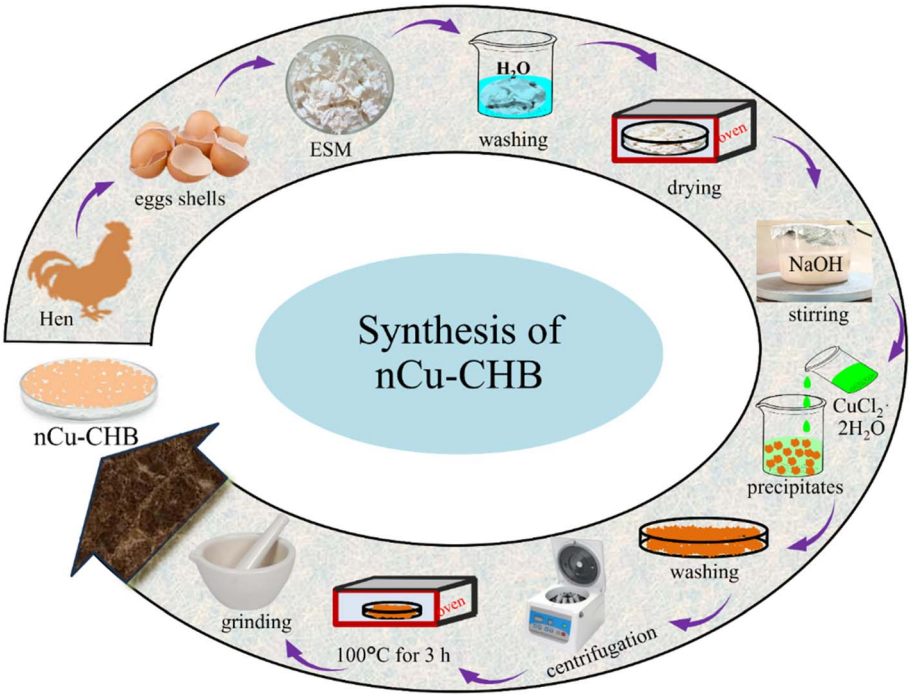

Scheme 1 Synthesis of nCu-CHB by chemical precipitation method.

2.4 Material characterization

The surface functional groups of the composites were analyzed by Fourier transform infrared spectroscopy (FTIR, Bruker IFS 66) within the 400–4000 cm^{-1} range using KBr pellet method. The structural properties were examined by X-ray diffraction (XRD) using Shimadzu XRD-6000 diffractometer equipped with Cu Kα radiation (λ = 0.154 nm) operated at 40 kV. The diffraction data were collected over a 2θ range of 10–80° with a scanning rate of 0.02° s^{-1}. For UV-visible analysis, UV-visible spectrometer (Lambda 600, PerkinElmer, USA) was used in the wavelength range of 200–800 nm. The morphology of the synthesized samples was examined using scanning electron microscopy (SEM, Hitachi S-4700), at an accelerating voltage of 15 kV and transmission electron microscopy (TEM, JEOL JEM-2100), operated at 200 kV. Chemical compositions and elemental states were analyzed using X-ray photoelectron spectroscopy (XPS, ESCALAB MK II) with Al Kα radiation (1486.6 eV) as the excitation source. The specific surface area was determined using Brunauer–Emmett–Teller (BET) analysis on a micrometrics, ASAP 2020 instrument, after degassing sample at 150 °C for 6 h and Barrett–Joyner–Halenda (BJH) method was applied to calculate the pore size distribution. Thermal stability of the sample was characterized by thermogravimetric analysis (TGA, NETZSCH STA 449F3) under nitrogen flow employing a heating rate of 10 °C min^{-1} from ambient temperature to 800 °C.

2.5 Photocatalytic activity

For photocatalytic testing, 10 mg of the synthesized nCu-CHB was dispersed into 50 mL of a 10 ppm MB solution in a 100 mL beaker at neutral pH. Before initiating the photocatalytic reaction, the suspension was agitated in the dark for 30 min to establish adsorption–desorption equilibrium between MB molecules and the catalyst surface. Photocatalytic experiments were conducted under visible-light exposure provided by 500 W xenon (Xe) lamp with 400 nm UV cut-off filter to eliminate UV radiation. The lamp was positioned 20 cm from the reactor, and the light intensity at the solution surface was measured to be 612.45 W m^{-2}. The temperature of the reaction system was maintained at 25 °C using a circulating water jacket to avoid heat influence. To monitor the photodegradation of dye, 3 mL aliquots of suspension were withdrawn at 15 min intervals, and the suspended catalyst particles were separated by high-speed centrifugation. The supernatant was then analyzed using a UV-visible spectrophotometer (UV-1800, Shimadzu, Japan), over the wavelength range of 200–800 nm. All the photocatalytic degradation experiments were conducted in triplicate to ensure reproducibility, and results are reported as mean ± standard deviation (SD) of three independent measurements. The degradation efficiency was determined using eqn (1);

$$\%\ \text{Photodegradation}(\eta) = \frac{C_o - C_t}{C_o} \times 100 \quad (1)$$

where, C_0 and C_t denote the concentration of MB before irradiation and at time t of photodegradation, respectively. A control experiment was also performed under identical visible light irradiation conditions without the catalyst to evaluate self-sensitized degradation of MB. Furthermore, the influence of critical operational parameters such as nCu-CHB dosage, MB concentration, and pH of solution on photocatalytic

performance was systematically investigated and the reaction conditions were optimized accordingly.

Additionally, radical trapping experiments were systematically conducted under identical photocatalytic condition to elucidate the role of reactive species such as superoxide radicals ($O_2^{\bullet-}$), electrons (e^-), holes (h^+), and hydroxyl radicals ($^{\bullet}OH$), involved in MB degradation using nCu-CHB. Specific scavengers were added individually at a concentration of 1 mM to identify the corresponding reactive species: $AgNO_3$ for e^-, ammonium oxalate for h^+, IPA for $^{\bullet}OH$ and *p*-BQ for $O_2^{\bullet-}$. The pH of the reaction solution was maintained at approximately 7, using 1 M HCl and NaOH solutions to ensure consistency with optimized photocatalytic conditions. The degradation efficiency was monitored under same irradiation time (90 min). Control experiments were conducted without any scavenger as a reference to accurately evaluate the influence of each trapping agent and ensure the reliability of the mechanistic analysis.

3 Results and discussion

3.1 Structural analysis

The XRD patterns of pristine ESM and synthesized nCu-CHB are presented in Fig. 1a. The diffraction pattern of ESM shows a broad hump centered at approximately 23°, which is attributed to the amorphous nature of protein fibers, rich in functional groups such as amides, amines, and carboxylic groups.[38] After copper incorporation, the nCu-CHB composite retained the broad amorphous hump characteristic of ESM. However, noticeable changes in the diffraction intensity along with the appearance of weak additional peaks in the nCu-CHB suggest structural modification due to copper incorporation, and its interaction with the various functional groups within the ESM matrix. Importantly, no sharp distinct peaks of crystalline CuO or Cu_2O were observed, indicating that Cu species were well dispersed and coordinated within the amorphous ESM matrix. A peak observed at 29.4° in both ESM and nCu-CHB samples corresponds to residual $CaCO_3$, likely due to the presence of residual eggshell components.[39] These observations suggest that copper is integrated into the ESM matrix through chemical interaction rather than simple physical deposition.

FTIR analysis of both ESM and nCu-CHB (Fig. 1b) was conducted to assess changes in the functional groups of ESM after copper incorporation. A characteristic broad band at 3433 cm^{-1} in ESM is associated with stretching vibration of O–H and N–H groups, commonly referred to as amide A. The absorption bands at 2924 cm^{-1} and 2850 cm^{-1} are assigned to the asymmetric stretching vibrations of –CH and $=CH_2$ groups, characteristic of amide B.[40] Upon Cu incorporation, the N–H and O–H stretching band shifts from 3443 cm^{-1} in ESM to 3451 cm^{-1} in nCu-CHB along with noticeable broadening and reduced intensity.[41] A prominent peak at 1635 cm^{-1} is attributed to the stretching vibration of C=O group, which corresponds to the amide I band of the glycoprotein in the ESM. After copper incorporation, this peak shifts to 1624 cm^{-1} with reduced intensity. This red shift indicates interaction between Cu^{2+} ions with oxygen atom of C=O bond, leading to weakening of the C=O bonds in the peptide chain, and confirming chemical bonding rather than physical adsorption.[42] Furthermore, two new peaks at 1116 cm^{-1} and 1262 cm^{-1} were observed in nCu-CHB, which correspond to the formation of new bonds between $-COO^-$ and metal ions.[43] Additionally, the weak absorption bands in the range of 498–618 cm^{-1}, further confirms Cu–O and Cu–N bond formation.[44–46] These spectral changes demonstrate the chemical interaction of Cu^{2+} within the functionalized ESM matrix.

Surface chemical composition and oxidation state of nCu-CHB were investigated using XPS. The full scan spectrum (Fig. 2a) indicates the existence of O, C, and Cu elements, demonstrating that copper has been successfully integrated into the ESM-derived matrix. Compared with literature-reported XPS spectra of pristine ESM,[34] which typically exhibit C 1s and O 1s peaks originating from protein functional groups, the emergence of additional Cu 2p signals at 933.7 eV confirms the successful incorporation of copper into the ESM matrix. The binding energies of 284.6 eV and 530.1 eV correspond to the C 1s and O 1s, peaks respectively. The O 1s spectrum (Fig. 2b) was deconvoluted into two components centered at 529.9 eV and 530.7 eV corresponding to Cu–O bonding and surface hydroxyl group (–OH)/oxygen-containing groups respectively. The high-resolution Cu 2p spectrum (Fig. 2c) displays characteristic Cu

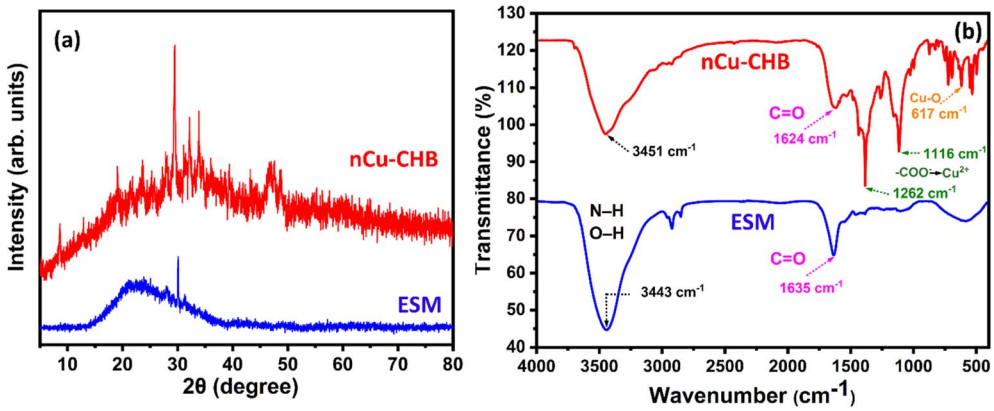

Fig. 1 (a) XRD and (b) FTIR spectra of the ESM and nCu-CHB.

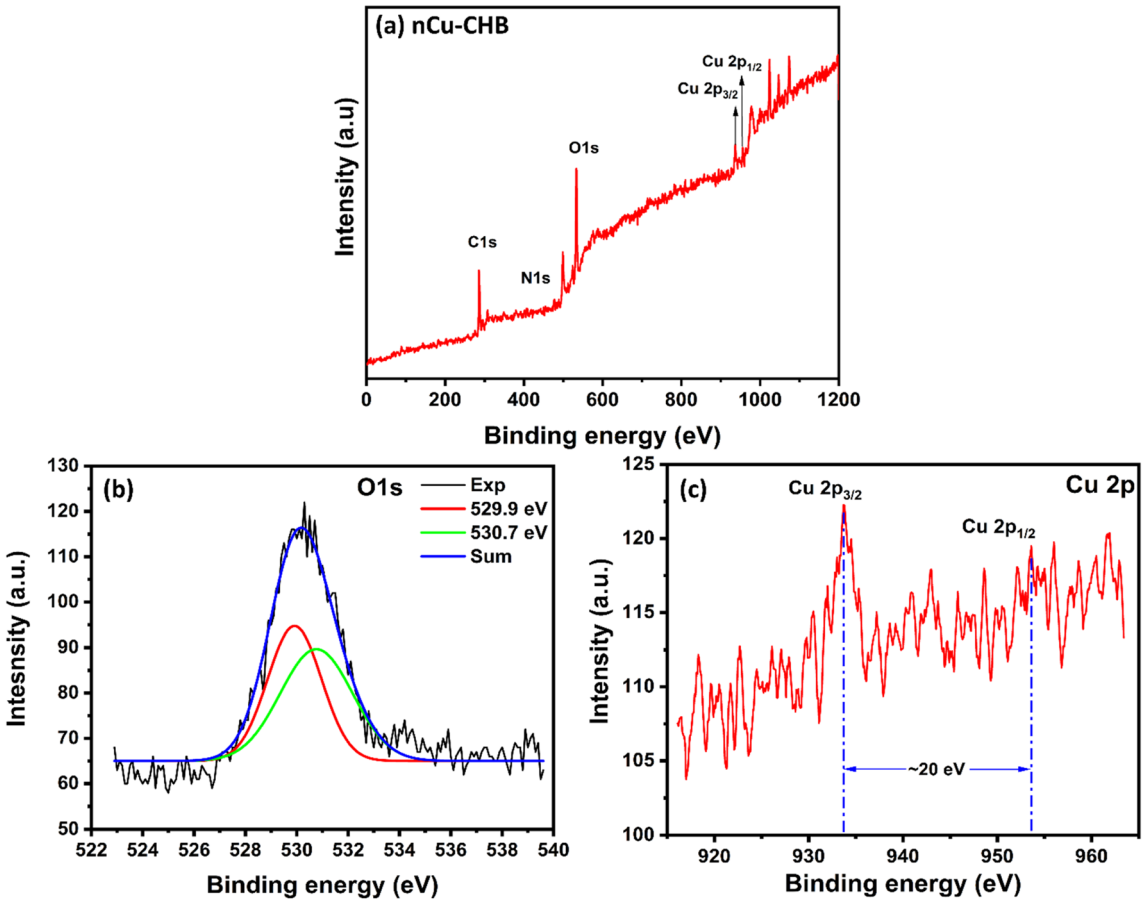

Fig. 2 (a) XPS survey spectrum and high-resolution spectra of (b) O 1s (c) Cu 2p of nCu-CHB.

$2p_{3/2}$ and Cu $2p_{1/2}$ peaks at 933.7 eV and 953.6 eV, respectively with spin–orbit splitting of approximately 20 eV. These binding energy values agree well with those of reported for Cu^{2+} species in the literature, suggesting the presence of oxidized copper coordinated within the biopolymeric matrix.[47] The Cu–O contribution further indicates chemical interaction between Cu^{2+} ions and oxygen containing functional groups (–COO– and –OH) of hydrolyzed ESM matrix. These findings suggest that copper is chemically bonded within the polymeric framework rather than physically adsorbed on the surface.

3.2 Morphological analysis

The morphological characteristics of nCu-CHB were examined using SEM and TEM. The SEM images of nCu-CHB reveal an interconnected hierarchical porous and wrinkled structure composed of irregularly shaped, crumpled sheet-like fragments (Fig. 3a). At higher magnification (Fig. 3b), nanoscale pores (~50.6 nm) and curved layered regions can be observed, clearly displaying a wrinkled surface texture. This morphology, typical processed biomaterial-derived materials, contributes to a large surface area and accessibility of active sites. Additionally, nanoscale cavities are distributed throughout the structure, which further improve the porosity and functional properties. These features are well-suited for photocatalytic application.[48,49]

The compositional analysis of nCu-CHB was examined *via* EDX spectrum (Fig. 3c) and it confirms the presence of key elements including C, O, Cu, and several other trace metals. The dominant peaks of C and O reflect the organic matrix of ESM, while multiple copper peaks verify successful metal incorporation. Fig. 3d and e represent the TEM images of nCu-CHB, revealing that copper particles are evenly distributed throughout the matrix, while slight agglomerations were also observed. The particles ranged from 5–9 nm with an average diameter of 5.45 nm as shown in (Fig. 3f).[50] The protein matrix surrounding the copper ions suggests that the copper species are likely interacting with the protein, possibly through binding or coordination.

3.3 Surface area analysis

To determine the adsorption capacity of nCu-CHB toward organic pollutants, BET and BJH methods were employed to evaluate the surface area and pore size distribution. These properties were examined *via* nitrogen adsorption–desorption isotherm at 77 K, displayed in Fig. 4a. The isotherms can be found to be classical type IV, having H3 type hysteresis loop.[51,52] The observed isotherm profile is indicative of mesoporous material, exhibiting characteristic pore diameters between 2–50 nm.[53] The BET surface area of nCu-CHB was found to be

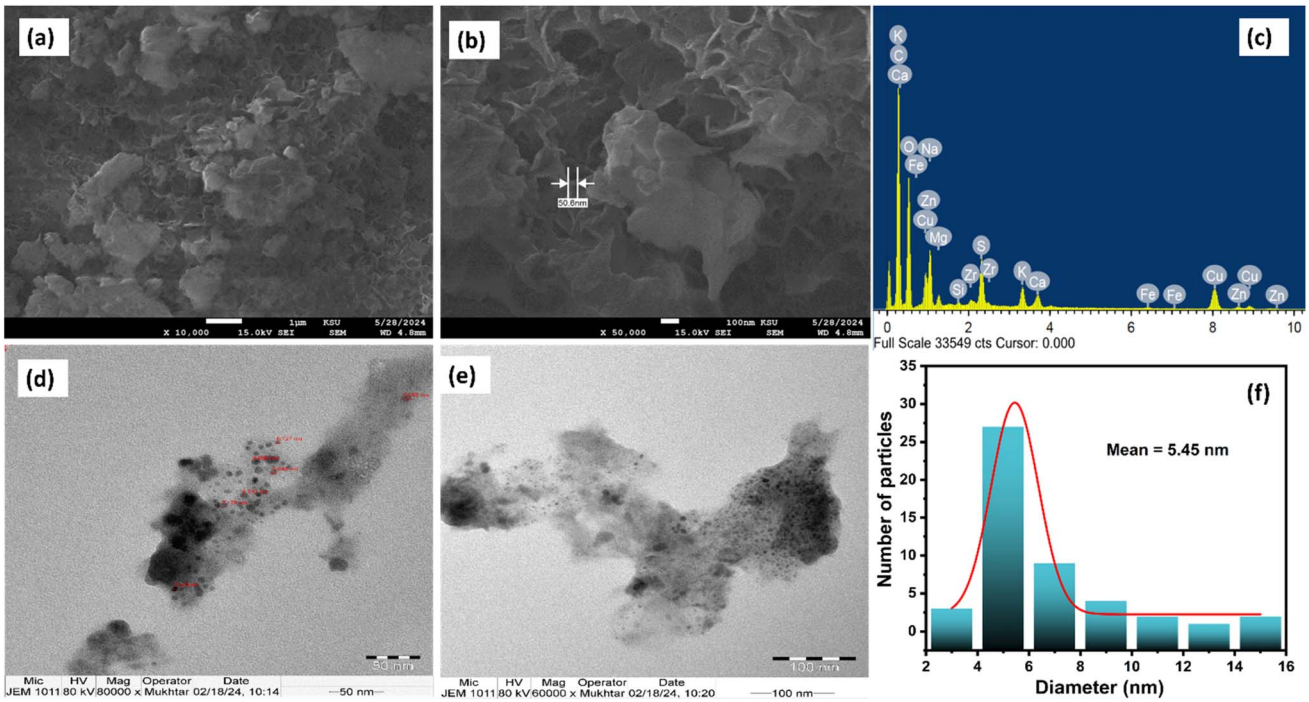

Fig. 3 SEM images at (a) 1 μm (b), 100 nm, (c) EDX, TEM images at (d) 50 nm (e) 100 nm and (f) histogram profile of nCu-CHB.

14.25 $m^2 g^{-1}$. The pore diameter of 18.26 nm (Fig. 4b) confirms the mesoporous nature of the material, and highest differential surface area appears around 20–50 A° (Fig. 4c), reinforcing the small mesopores dominate the surface of the nCu-CHB.

3.4 Optical analysis

The optical properties of ESM and nCu-CHB were examined by UV-visible absorption spectroscopy, and the spectra of both samples are presented in Fig. 5a and b. The absorption spectra of ESM exhibit notable peaks at 240 and 280 nm which can be attributed to n–π^* and π–π^* transitions of the chromogenic moieties, including carbonyl groups and aromatic amino acids (tryptophan and tyrosine), respectively.[54,55] In nCu-CHB spectrum, a broad band around 306 nm is observed, which can be attributed to metal–ligand charge transfer transitions.[56] Additionally, a broad band at approximately 800 nm corresponds to d–d transitions of Cu^{2+} (d^9 configuration).[57,58] However, the observed band shift and appearance of new absorption maxima confirm strong electronic interaction between Cu^{2+} ions and ESM protein functional groups. Furthermore, the semiconducting properties of the ESM and synthesized nCu-CHB were evaluated by calculating the band gap energy (E_g), using Tauc's formula, as expressed in eqn (2).[59]

$$(\alpha h\nu)^2 = A(h\nu - E_g) \quad (2)$$

where, α refers to the absorption coefficient, ν is the frequency of incident light, h is Plank's constant, A is the proportionality constant, and E_g represents the energy band gap. The band gap values of the ESM and nCu-CHB were calculated by plotting

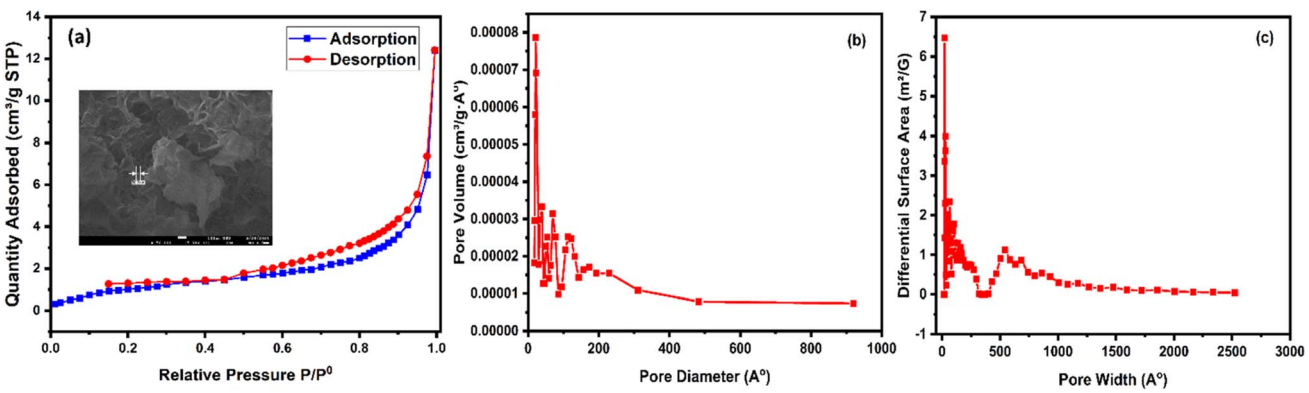

Fig. 4 (a) BET plot and (b and c) pore size distribution of nCu-CHB.

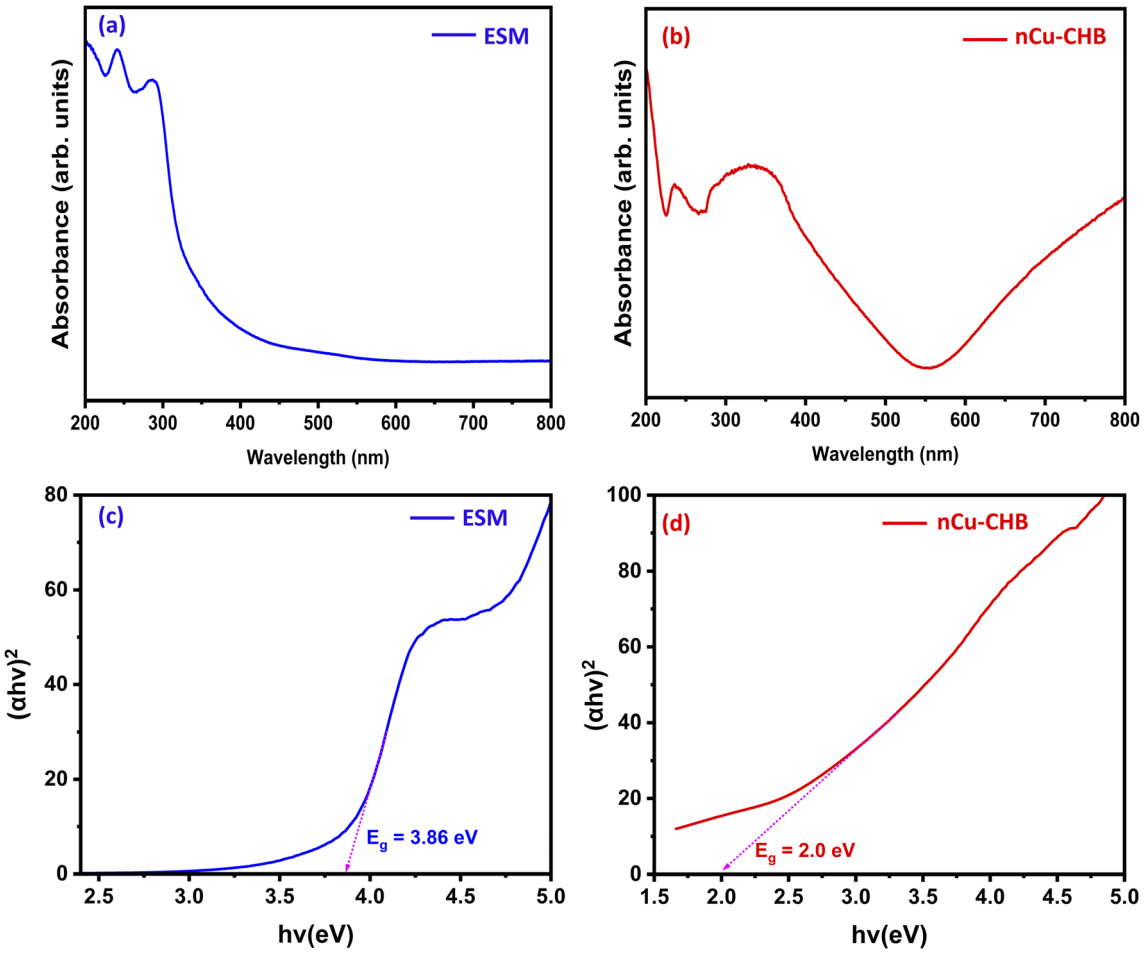

Fig. 5 (a and b) Absorbance spectra, Tauc plots of (c) ESM (d) nCu-CHB.

$(\alpha hv)^2$ *versus* hv, as illustrated in Fig. 5c and d. The energy band gap (E_g) decreased from 3.86 eV (ESM) to 2.0 eV (nCu-CHB). This significant band gap narrowing in nCu-CHB is likely due to the incorporation of Cu ions, which may cause delocalization of electronic states near the Fermi level.[60] These results suggest that nCu-CHB exhibits enhanced semiconducting behavior, making it an efficient photocatalytic material for effective degradation of dyes and other organic pollutants. While UV-visible analysis provides insight into band gap and light absorption properties, further investigation using photoluminescence (PL) spectroscopy would be beneficial to directly evaluate charge carrier recombination behavior.

3.5 Thermal analysis

TGA-DTG was performed to investigate the thermal resistance of nCu-CHB. Fig. 6 shows a multistage decomposition process with the inflection points at 76, 122, 240, 315 and 705 °C. The initial mass loss of ~8% occurring between 35 °C and 194 °C can be associated with the desorption of physically adsorbed water and collagen denaturation.[6,61] A further increase in temperature from 194 °C to 325 °C causes weight loss of 14% as a consequence of the thermal degradation of collagens, amino acids and peptides into volatile compounds.[62,63] A plateau was observed between 325 °C and 800 °C correspond to the slow and gradual decomposition of the organic matrix and weight loss of 36% was observed at this stage.[6] After several steps of pyrolysis,

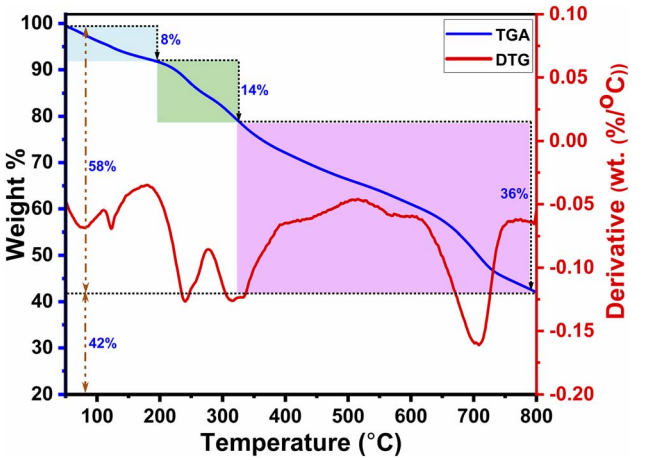

Fig. 6 TGA with DTG curve of nCu-CHB.

the remaining 42% mass above 800 °C indicates a higher degree of copper-stabilized collagen in the nCu-CHB.[64,65]

4 Photocatalytic activities

The visible-light irradiated photocatalytic activity of nCu-CHB was systematically assessed for MB degradation. A blank photolysis experiment performed under identical visible-light conditions without catalyst (Fig. 7a) showed only 9.15% degradation after 90 min, confirming that self-sensitized degradation is negligible. In contrast, significant degradation was observed in the presence of photocatalyst. Prior to visible-light irradiation, the suspension was kept under magnetic stirring in the absence of light to allow equilibrium between dye adsorption and desorption on catalyst surface. The time-dependent UV-vis spectral changes and photocatalytic degradation profiles of MB are shown in Fig. 7a–c. The absorbance band of MB decreases significantly with increasing irradiation time in the presence of photocatalysts. The nCu-CHB exhibited degradation efficiency of 88.75%, markedly higher than that of pristine ESM which showed only 20.21%, demonstrating its superior photocatalytic performance. This enhanced photocatalytic activity is primarily associated with electronic structure modification and redox properties introduced by Cu incorporation. The significant reduction in band gap energy (from 3.86 eV for ESM to 2.0 eV for nCu-CHB) strengthens of visible-light harvesting and assists in the generation of photoinduced charge carriers.

In addition, the enhanced photocatalytic performance of nCu-CHB can be attributed to the functional groups present in the ESM matrix, which provide abundant active sites for adsorption of MB molecules. The adsorption of MB on the catalyst surface is primarily governed by electrostatic interactions, hydrogen bonding, and π–π interactions, depending upon the surface charge and functional groups chemistry.[30,66] Under neutral conditions, cationic MB strongly interacts with negatively charged $-COO^-$ groups *via* electrostatic interaction. Furthermore, $-NH_2$ and –OH groups facilitate adsorption *via* hydrogen bonding, promoting effective anchoring of MB molecules on catalyst surface. In addition, π–π interaction may occur between the aromatic rings of MB and aromatic amino acid residues (*e.g.*, tryptophan and tyrosine) present in the proteinaceous structure of ESM. Thus, the overall performance of nCu-CHB arises from the synergistic interplay between adsorption processes governed by surface functional groups and photocatalytic activity induced by Cu-mediated electronic structure modification. The kinetics of MB photodegradation were analyzed using eqn (3).

$$\ln\frac{C_0}{C_t} = kt \tag{3}$$

where "k" is the rate constant and "t" is the time.

Fig. 7d depicts the C_t/C_o *vs.* irradiation time plots for ESM and nCu-CHB, revealing the highest degradation rate of MB with nCu-CHB. As depicted in Fig. 7e, a linear correlation between $\ln(C_t/C_o)$ and irradiation time indicates that the photodegradation follows pseudo-first-order kinetics with regression coefficients (R^2) of 0.9413 for ESM and 0.9931 for nCu-CHB. The rate constants for ESM and nCu-CHB (Fig. 7f) were

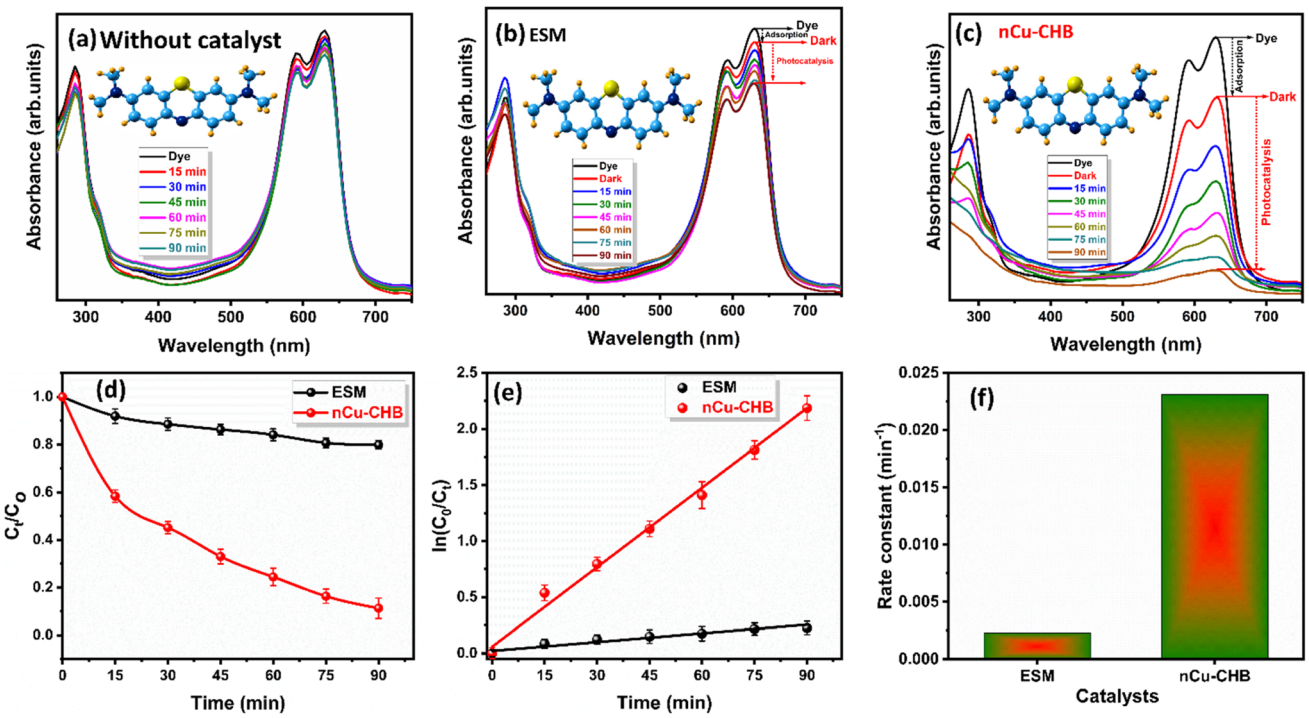

Fig. 7 UV-vis absorbance spectra of MB under visible-light irradiation (a) without catalyst (b) in the presence of ESM (c) in the presence of nCu-CHB (d and e) kinetic plots and (f) rate constants. Error bars represent standard deviation of triplicate experiments performed under identical conditions.

calculated to be 0.0023 min^{-1}, and 0.0231 min^{-1} respectively, demonstrating nearly a tenfold increase in reaction rate upon Cu incorporation. To further optimize reaction conditions for MB degradation using nCu-CHB, several factors including initial dye concentration, catalyst dose, solution pH were studied. The pH of dye solution was precisely controlled through dropwise addition of 1 M NaOH or HCl solutions. To evaluate the practical efficiency of the synthesized composite, its photocatalytic performance was compared with the previously reported catalysts and comparative data are summarized in Table 1.

4.1 Effect of MB concentration

The influence of MB concentration (10–40 ppm) using nCu-CHB was systematically investigated under controlled conditions, catalyst dose of 10 mg, and 90 min of visible-light exposure at neutral pH. The results depicted in Fig. 8a reveal an inverse correlation between initial pollutant load and degradation efficiency. The degradation efficiency decreased from 88.74% to 57.53% with the increase in initial concentration from 10 to 40 ppm, as depicted in Fig. 8b. This decline in degradation efficiency can be attributed to the binding of dye molecules on nCu-CHB surface, which results in a lesser penetration of photons to the surface of the photocatalyst.[67] Furthermore, the saturation of dye solution causes absorption of photons by dye molecules, which ultimately results in a lower photoexcitation rate of the catalyst.[68] Hence, the generation of $O_2^{\bullet -}$ and $OH^{\bullet}$ radicals was reduced, resulting in decreased photocatalytic activity.[44] Fig. 8c demonstrates the kinetic graph of MB degradation and the estimated reaction rate constants for the degradation of 10, 20, 30, and 40 ppm of MB are 0.0230 min^{-1}, 0.0160 min^{-1}, 0.0104 min^{-1}, and 0.0093 min^{-1}, respectively, and the correlation coefficients (R^2) are 0.9942, 0.9912, 0.9809, and 0.9911, respectively. Fig. 8d shows the absorbance plot of MB degradation by nCu-CHB at the optimized MB concentration.

4.2 Effect of catalyst dose

To avoid inappropriate use of catalyst and to determine the optimal catalyst dosage for efficient MB degradation, experiments were carried out at different dosages (5, 10, 15, and 20 mg) of nCu-CHB in 50 mL of a 10 ppm MB solution at pH 7 under visible-light irradiation for 90 min. Fig. 9a illustrates the influence of catalyst dose on the photocatalytic reaction; as the dose increases, the concentration of MB dye decreases with time. Increasing the nCu-CHB dose from 5 mg to 15 mg resulted in an increase in degradation efficiency from 78.62% to 98.09% as shown in Fig. 9b. The presence of a large amount of catalyst provides more accessible active sites for the adsorption of dye molecules. Consequently, the generation of electron–hole pairs (e^-/h^+) increases with higher catalyst loading due to enhanced interaction with light irradiation. These e^-/h^+ pairs interact with water and dissolved oxygen to generate free radicals, resulting in further degradation of the MB dye.[69] A further increase in catalyst dose to 20 mg resulted in a slight decrease in percentage degradation. This observation indicates that 15 mg is found to be a more critical dose with 98.09% degradation efficiency under irradiation of visible-light for 90 min. Further, the reaction kinetics of MB degradation over nCu-CHB and the corresponding rate constants were determined. The results depicted in Fig. 9c showed a linear relation between $\ln(C_o/C)$ *vs.* irradiation time (min), indicating that the photocatalytic degradation of MB over nCu-CHB is satisfied through pseudo-first-order kinetics. At doses 5, 10, 15, and 20 mg of nCu-CHB, the reaction rate constants were 0.0176, 0.0231, 0.0432, and 0.0357 min^{-1}, respectively, and the correlation coefficients (R^2) were 0.9980, 0.9898, 0.9975, and 0.9951, respectively. Fig. 9d shows the time-dependent UV-vis absorbance data for MB degradation using 15 mg of nCu-CHB.

4.3 Effect of pH

The pH of the reaction medium significantly affects the degradation of MB dye. A systematic investigation of pH influence on the photocatalytic activity of nCu-CHB was conducted using 10 mg of nCu-CHB in 10 ppm of MB solution at different pH values, ranging from 3 to 11, under visible-light irradiation for 60 min. The solutions pH was controlled through the gradual addition of 1 M NaOH and HCl solutions. Fig. 10a shows the UV-vis spectral profile of MB degradation in the presence of nCu-CHB at various pH values. The results shown in Fig. 10b reveal that dye degradation is relatively low in acidic medium, while it improves significantly under basic medium. The percentage degradation of dye increases from 13.75% at pH 3 to 75.72% as the pH of the solution rose to 7, reaching a maximum of 93.04% at pH 11. This drastic change in catalytic activity can be attributed to the catalyst surface charge and the ionic nature of the dye.[70] In acidic conditions, the proton-rich medium leads to the protonation of carboxylic acid (–COOH) and amine

Table 1 Comparison of degradation efficiency of nCu-CHB with other reported studies

Catalysts	Pollutant	Concentration (mg L^{-1})	Light source	Catalyst dose (g L^{-1})	Time (h)	Degradation efficiency (%)	Ref.
ES/TiO_2	MB	1.44	UV	5.0	24	95.6	71
ESM/Cu_2O	MB	30	Visible	0.40	1.0	97.0	34
TiO_2-PEI-ESM	RhB	10	Visible	0.42	1.0	95.0	72
HAP/CuO/GEL	MB	20	Visible	0.5	2.0	90.8	73
BC/MoS_2/TiO_2	MB	10	Visible	—	2.0	91.2	74
CA/TiO_2	MB	10	Visible	0.30	5.0	85	75
nCu-CHB	MB	10	Visible	0.30	1.5	98.1	This study

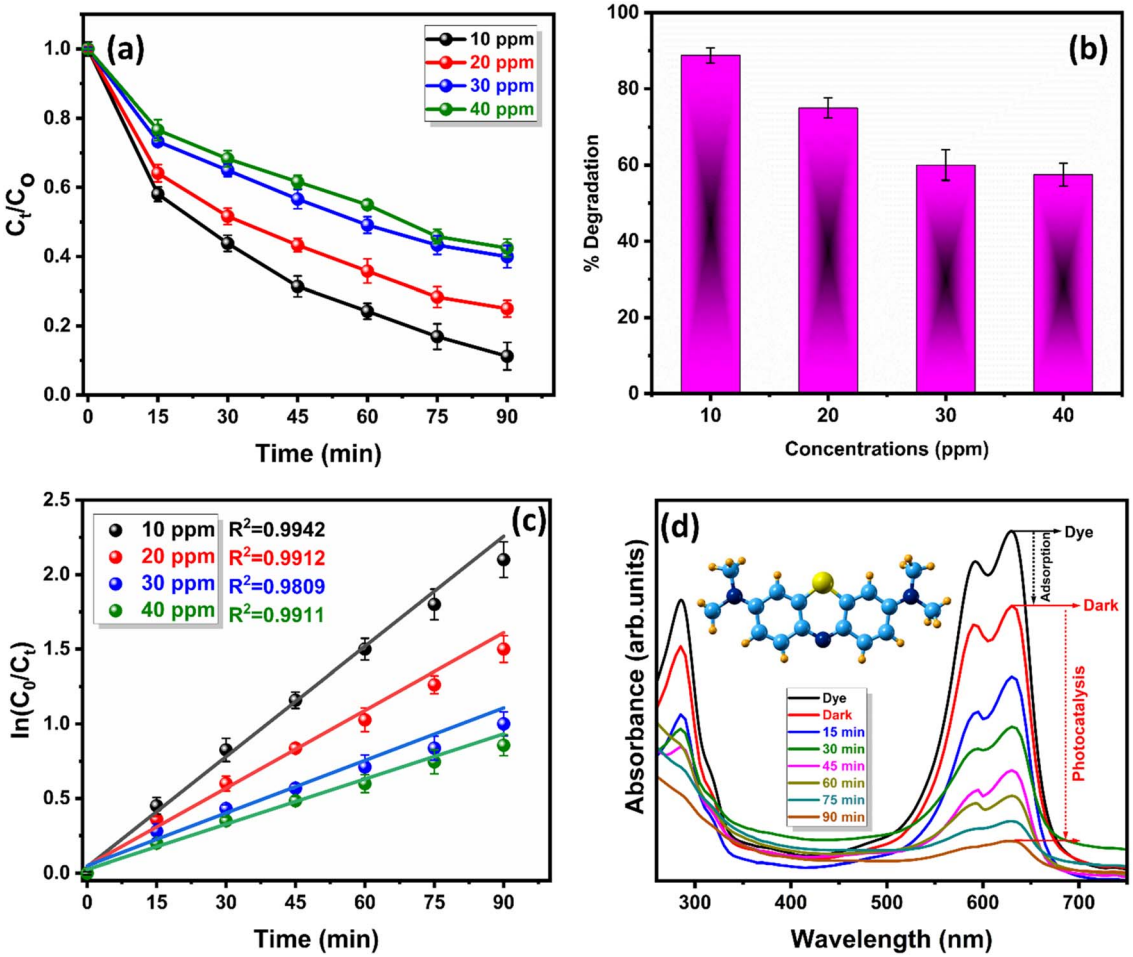

Fig. 8 Effect of MB concentrations on photocatalytic degradation using nCu-CHB: (a) kinetic plot of C_t/C_0 *vs.* time, (b) % degradation bar graph, (c) plot of ln C_0/C_t *vs.* time, and (d) absorbance spectra of MB dye (10 ppm) in the presence of nCu-CHB. Error bars represent standard deviation of triplicate experiments performed under identical conditions.

groups (–NH_2) on the photocatalyst. Since the MB is a cationic dye, it is repelled by the positively charged surface of the photocatalyst, resulting in reduced dye adsorption and hence lower degradation. The increase in dye degradation from acidic to neutral pH is due to the presence of zwitterionic groups (–COO^-, –NH_3^+), where negatively charged carboxylate groups facilitate electrostatic interactions with the dye molecules and hence, increase the dye degradation. However, the maximum degradation is not achieved at neutral pH because the presence of positively charged –NH_3^+ groups still hinders the adsorption of dye onto the catalyst surface. Under basic conditions, the surface of the photocatalyst becomes predominantly negatively charged due to the deprotonation of carboxylic groups and the absence of –NH_3^+ groups. This electrostatic interaction between the catalyst surface and the dye molecules enhances adsorption and consequently improve photodegradation.[69]

4.4 Scavenger study

Radical scavenging experiments were systematically performed to investigate the role of dominant reactive oxygen species involved in MB degradation using nCu-CHB. The addition of *p*-BQ and IPA significantly suppressed the degradation efficiency (Fig. 11a), indicating that $O_2^{\bullet-}$ and $^{\bullet}OH$ were the dominant species responsible for MB degradation. In contrast the presence of $AgNO_3$ and OA resulted in a comparatively smaller reduction in degradation efficiency, suggesting that e^- and h^+ played secondary roles in the reaction mechanism.

4.5 Regeneration and stability

The stability and recyclability of the photocatalyst are essential for large-scale industrial applications. To evaluate the stability of nCu-CHB, three consecutive photocatalytic cycles were performed under identical optimized conditions (50 mL of 10 ppm MB solution, 10 mg catalyst, 90 min visible irradiation at neutral pH), and the degradation efficiency was measured after each run. After each cycle, the catalyst was filtered, rinsed, dried, and reused for the photocatalytic degradation. The results depicted in Fig. 11b demonstrate a slight decrease in the degradation efficiency after each subsequent run. After the third cycle, the degradation efficiency of nCu-CHB decreased by 11%, indicating that the reused photocatalyst still retains considerable activity. This slight decrease in degradation efficiency can

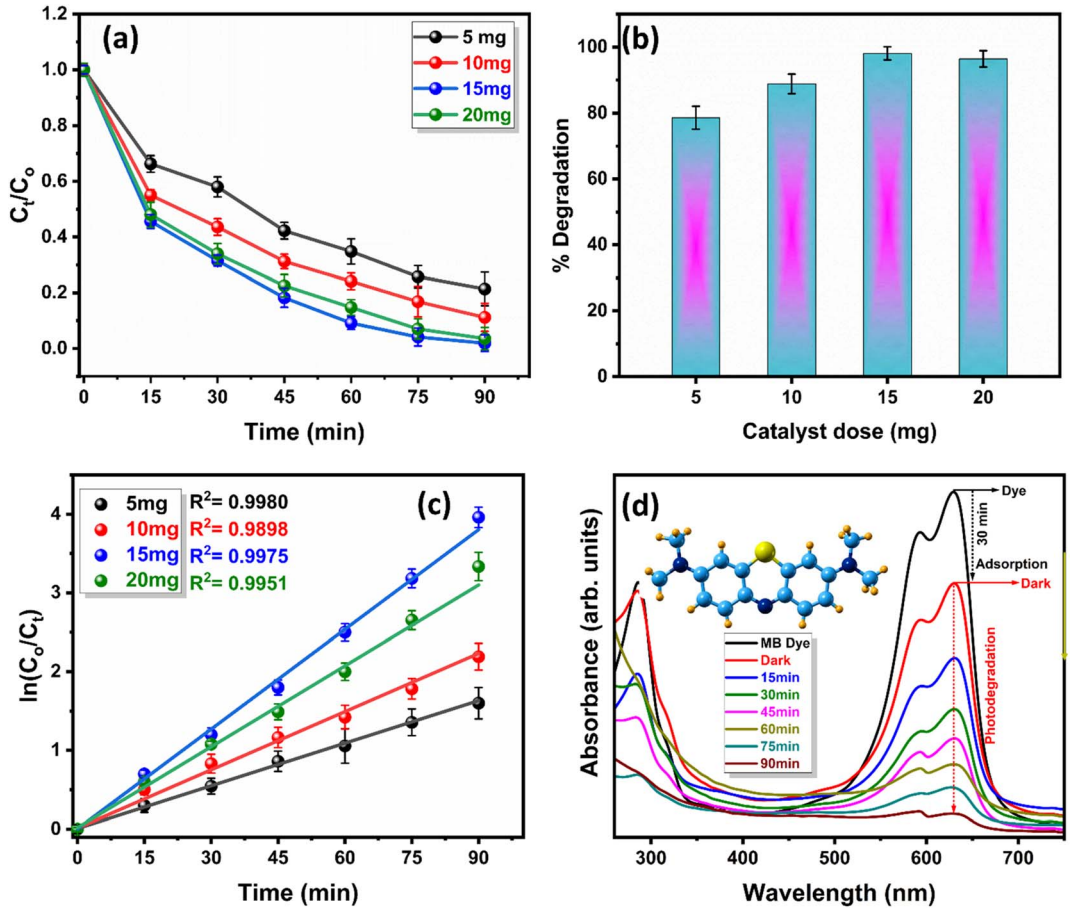

Fig. 9 Effect of catalyst dose on photocatalytic degradation using nCu-CHB (a) kinetic plot C_t/C_0 *vs.* time, (b) % degradation bar graph (c) plot of ln C_0/C *vs.* time and (d) absorbance spectra of MB dye (10 ppm) in the presence of nCu-CHB (15 mg). Error bars represent standard deviation of triplicate experiments performed under identical conditions.

be attributed to minor catalyst loss during recollection or inactivation of the active sites of the catalyst by adsorbed reaction intermediates.[44] To further examine the morphological stability, SEM images of nCu-CHB before and after photocatalytic degradation are presented in Fig. 11c and d. The hierarchical fibrous structure of the composite is largely preserved after the third cycle, with no significant structural collapse or severe aggregation observed. Minor surface roughness is visible, which may be associated with adsorption of reaction intermediates. These observations confirm that the nCu-CHB composite maintains reasonable structural integrity and stability during repeated photocatalytic experiments.

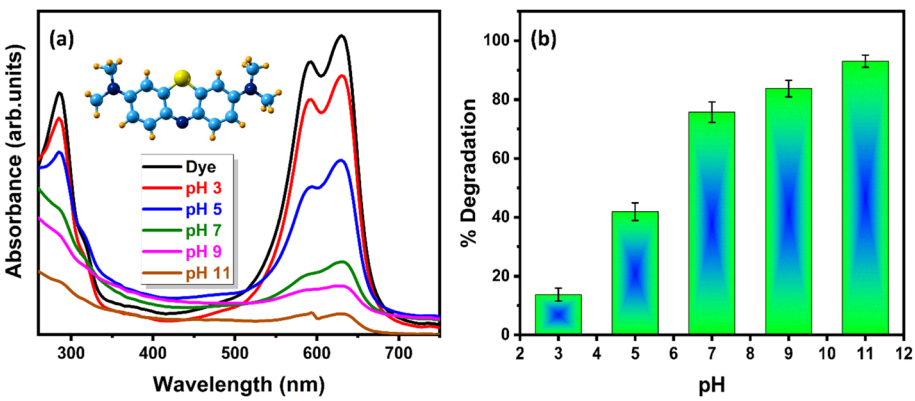

Fig. 10 Effect of pH on photocatalytic degradation of MB using nCu-CHB (a) absorbance spectra (b) bar graph of degradation (%) of nCu-CHB. Error bars represent standard deviation of triplicate experiments performed under identical conditions.

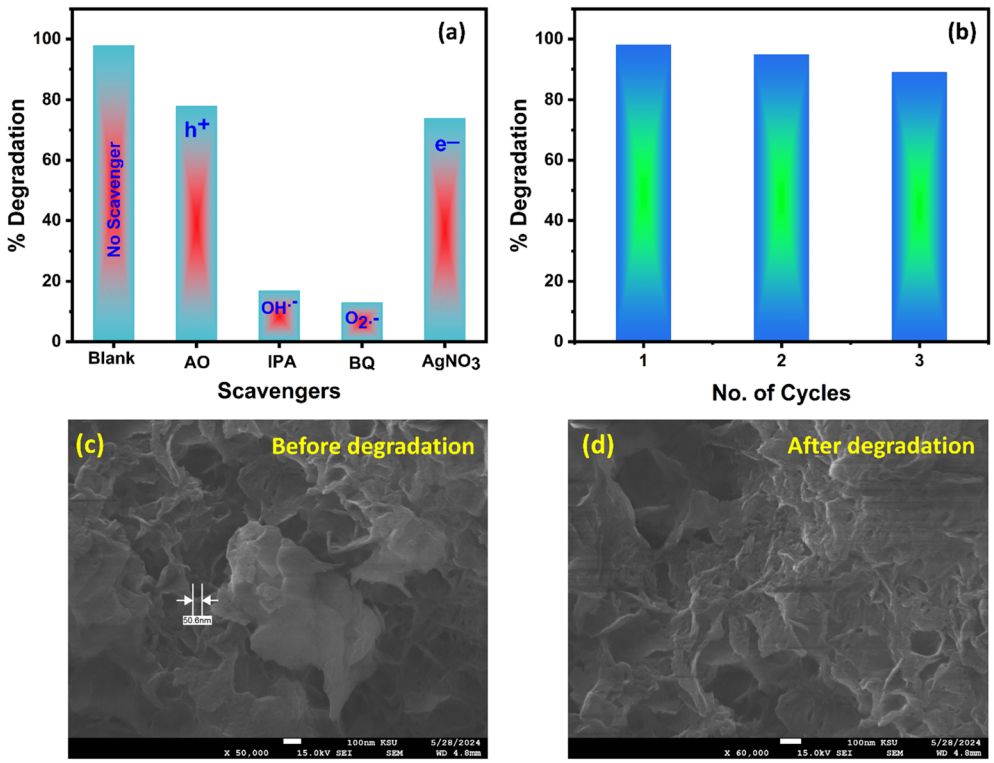

Fig. 11 (a) Scavenging tests (b) reusability, SEM images (c) before and (d) after photocatalytic degradation of MB using nCu-CHB.

4.6 Possible degradation mechanism

To gain insight into the possible photocatalytic degradation mechanism of MB using nCu-CHB, radical trapping studies were performed. The results revealed that IPA and *p*-BQ significantly suppressed the photocatalytic degradation of MB, reducing it to 17% and 13%, respectively. These findings indicate that $O_2^{\bullet-}$ and $^{\bullet}OH$ radicals play a dominant role in the degradation process as shown in Fig. 11a. Fig. 12 schematically illustrates the proposed photodegradation mechanism of MB over nCu-CHB. Visible-light photon with $E_g > 2.0$ eV induce VB-CB electronic transition in nCu-CHB, generating the e^-/h^+ pairs. The photoexcited electrons in the CB can participate in the reduction of dissolved oxygen to generate $O_2^{\bullet-}$, while the corresponding holes in the VB are highly oxidative species and can react with hydroxyl groups or hydroxide ion to form $^{\bullet}OH$ radicals. These reactive species play a key role in the efficient degradation of MB dye into less harmful products like water and carbon dioxide. The whole mechanism has been illustrated in the following eqn (4)–(7).

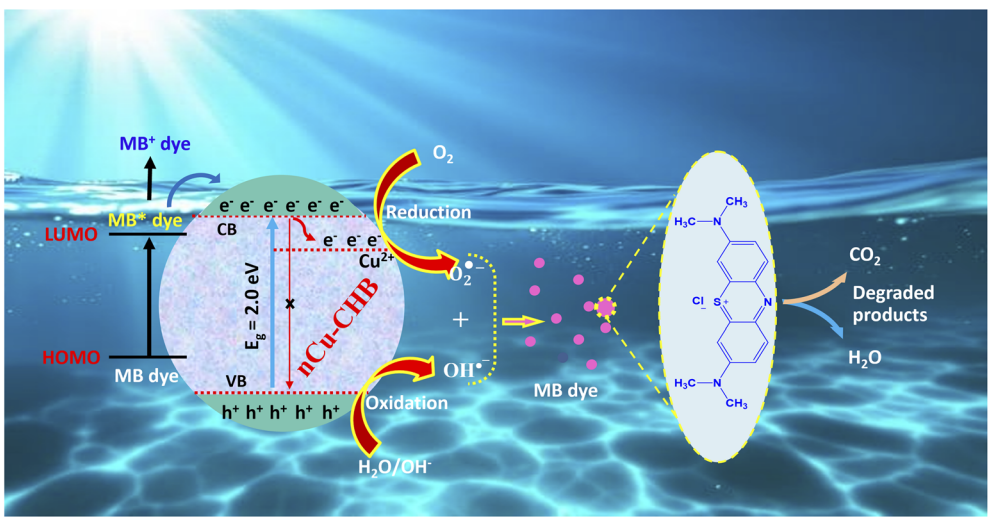

Fig. 12 Proposed degradation mechanism of MB over nCu-CHB.

$$\text{nCu-CHB} + h\nu \rightarrow \text{nCu-CHB}\,[e^-_{(CB)} + h^+_{(VB)}] \quad (4)$$

$$\text{nCu-CHB}\,(h^+_{VB}) + OH^- \rightarrow {}^{\bullet}OH + \text{nCu-CHB} \quad (5)$$

$$\text{nCu-CHB}\,(e^-_{CB}) + O_2 \rightarrow O_2^{\bullet -} + \text{nCu-CHB} \quad (6)$$

$$MB + OH^{\bullet -}/O_2^{\bullet -} \rightarrow CO_2 + H_2O + \text{degraded products} \quad (7)$$

5 Conclusion

In summary, the nCu-CHB photocatalyst was fabricated from ESM hydrolysate *via* a simple chemical precipitation method, and the material was characterized by advanced characterization techniques. Structural and spectroscopic analysis confirmed the successful incorporation of Cu species within the biopolymeric matrix and indicated modification of the electronic structure of ESM after copper coordination. The resulting material, with a reduced band gap and porous morphology, demonstrated effective visible-light photocatalytic degradation of MB (98.09%), following pseudo-first-order kinetics. The improved photocatalytic activity can be attributed to the synergistic effects of copper incorporation and the functionalized porous structure of the ESM matrix, which enhance light absorption and promotes adsorption–photocatalysis interaction. Overall, this study highlights the potential of waste-derived biopolymers as sustainable matrices for developing metal-chelated photocatalysts for environmental remediation.

Conflicts of interest

There are no conflicts to declare.

Data availability

Data will be available on request.

Acknowledgements

This work was funded by Ongoing Research Funding program (ORF-2025-442), King Saud University, Riyadh, Saudi Arabia.

References

1 A. A. Alothman, A. Ayub, S. K. Hachim, B. M. Mohammed, F. Hussain, M. Altaf, Z. J. Kadhim, H. A. Lafta, Y. S. Alnassar, M. A. Shams, N. A. Almuhous, M. Ouladsmane and M. Sillanpaa, *Environ. Sci. Pollut. Res.*, 2023, **30**, 37332–37343.
2 T. B. Mbuyazi and P. A. Ajibade, *RSC Adv.*, 2025, **15**, 6400–6412.
3 K. Parchami, N. Habibzadehnesami, A. Pirkarami, S. Haghighat-Nezhad, N. Gheitasi, M. S. Nabavi and E. Ghasemi, *Environ. Res.*, 2025, **279**, 121741.
4 S. Goudjil, S. Guergazi, D. Ghernaout, D. Temim and T. Masmoudi, *Desalin. Water Treat.*, 2024, **319**, 100539.
5 J. Zhao, X. Wen, H. Xu, Y. Weng and Y. Chen, *Environ. Technol.*, 2021, **42**, 4380–4392.
6 X. He, D. P. Yang, X. Zhang, M. Liu, Z. Kang, C. Lin, N. Jia and R. Luque, *Chem. Eng. J.*, 2019, **369**, 621–633.
7 R. Alabada, A. Ayub, Y. Ajaj, S. I. Bhat, R. H. Alshammari, A. Abduldayeva, A. I. Mallhi, Z. Ahmad and R. M. K. Mohamed, *J. Alloys Compd.*, 2024, **977**, 173400.
8 S. K. Brar, G. K. Soni, A. Bharti, Neelam, N. Wangoo and R. K. Sharma, *Mater. Sci. Eng., B*, 2025, **318**, 118248.
9 A. Bhawsar, D. Bhutada and S. Ghuge, *J. Indian Chem. Soc.*, 2025, **102**, 101742.
10 A. H. Mian, S. Qayyum, S. Zeb, T. Fatima, K. Jameel and B. Rehman, *Environ. Technol. Innov.*, 2024, **34**, 103615.
11 Z. Gao, B. Ju, B. Tang, W. Ma, W. Niu and S. Zhang, *Langmuir*, 2024, **40**, 3231–3240.
12 S. Patel, A. T. Nair and A. R. Makwana, *Int. J. Environ. Sci. Technol.*, 2025, **22**, 477–488.
13 K. Abhisek, S. S. Vhatkar, H. T. Mathew, P. Singh and R. Oraon, *Discover Chem.*, 2025, **2**, 41.
14 K. K. Wang and P. V. Chai, *Next Nanotechnol.*, 2026, **9**, 100353.
15 A. Chauhan, R. Kumar, S. Devi, Sonu, P. Raizada, P. Singh, V. K. Ponnusamy, A. Sudhaik, A. K. Mishra and R. Selvasembian, *Surf. Interfaces*, 2024, **54**, 105152.
16 M. Maruthupandy, G. Rajivgandhi, T. Muneeswaran, S. Vasantharaj, G. Sandoval-Hevia, M. Muneeswaran and N. A. B. M. Radzi, *Int. J. Biol. Macromol.*, 2025, **307**, 142132.
17 L. Qomariyah, A. M. Rahmatika, E. H. Sanjaya, W. Widiyastuti, T. Hirano, T. Van Pham and N. R. Putra, *Int. J. Biol. Macromol.*, 2025, **305**, 141134.
18 S. Park, H. Sharma, M. Safdar, J. Lee, W. Kim, S. Park, H. E. Jeong and J. Kim, *Environ. Res.*, 2024, **250**, 118490.
19 P. Debnath and S. K. Ray, *Int. J. Biol. Macromol.*, 2025, **285**, 138228.
20 I. Hasan, A. Bassi and P. Kalakonda, *Surf. Interfaces*, 2025, **56**, 105456.
21 R. H. Jacob, A. S. Afify, S. M. Shanab and E. A. Shalaby, *Biomass Convers. Biorefinery*, 2024, **14**, 2907–2921.
22 M. Manimohan, S. Pugalmani, K. Ravichandran and M. A. Sithique, *RSC Adv.*, 2020, **10**, 18259–18279.
23 S. Dutta, C. B. Pohrmen, I. Banerjee, A. Trivedi, R. Verma and S. Dubey, *Octa J. Biosci.*, 2021, **9**, 30–36.
24 L. Li, T. Huang, S. He, X. Liu, Q. Chen, J. Chen and H. Cao, *RSC Adv.*, 2021, **11**, 18994–18999.
25 D. Xu, D. Liao, B. Xie, Y. Zhang, J. Sun, Z. Tong, L. Sun, Y. Zheng and G. Zhou, *Surf. Interfaces*, 2025, **56**, 105604.
26 R. G. Saratale, Q. Sun, V. S. Munagapati, G. D. Saratale, J. Park and D. S. Kim, *Chemosphere*, 2021, **281**, 130777.
27 J. Chen, X. Ji, Z. Huang, R. Zhang, L. Liu, R. Geng and Q. Ji, *Biomass Convers. Biorefinery*, 2025, **15**, 11851–11862.
28 H. Daraei, A. Mittal, J. Mittal and H. Kamali, *Desalin. Water Treat.*, 2014, **52**, 1307–1315.
29 Y. Yang, D. Gan, X. Li, J. Zhou, L. Yang, B. Dai and S. Xia, *J. Water Process Eng.*, 2024, **62**, 105249.
30 T. Siah, H. C. Yew Foo, I. S. Tan, Y. F. Yeong, M. K. Lam, K. T. Lee and M. K. Wong, *Sep. Purif. Technol.*, 2025, **370**, 133211.

31 S. Parvin, B. K. Biswas, M. A. Rahman, M. H. Rahman, M. S. Anik and M. R. Uddin, *Chemosphere*, 2019, **236**, 124326.
32 B. Pant, M. Park, H. Y. Kim and S. J. Park, *J. Alloys Compd.*, 2017, **699**, 73–78.
33 Q. Zhou, W. Huang, C. Xu, X. Liu, K. Yang, D. Li, Y. Hou and D. D. Dionysiou, *Chem. Eng. J.*, 2021, **420**, 129582.
34 T. Wu, J. Cao and X. Jiang, *Appl. Surf. Sci.*, 2023, **612**, 155752.
35 I. Ahmad, M. A. Aftab, A. Fatima, S. D. Mekkey, S. Melhi and S. Ikram, *Coord. Chem. Rev.*, 2024, **514**, 215904.
36 P. Sharma, S. Kar, M. Sahu and M. Ganguly, *RSC Adv.*, 2025, **15**, 27995–28020.
37 S. Ganesan, S. Subramani, D. Manoj, M. Elancheziyan, V. Manikandan, S. G. Ramakrishnan, S. L. Soundrya, S. Singh, D. Varshney and H. M. Lo, *Biomass Bioenergy*, 2025, **203**, 108266.
38 Y. Xin, C. Li, J. Liu, J. Liu, Y. Liu, W. He and Y. Gao, *R. Soc. Open Sci.*, 2018, **5**, 180532.
39 J. Li, D. Zhai, F. Lv, Q. Yu, H. Ma, J. Yin, Z. Yi, M. Liu, J. Chang and C. Wu, *Acta Biomater.*, 2016, **36**, 254–266.
40 M. K. Rath, B. H. Choi, M. J. Ji and K. T. Lee, *Ceram. Int.*, 2014, **40**, 3295–3304.
41 J. Choi, B. Pant, C. Lee, M. Park, S. J. Park and H. Y. Kim, *J. Ind. Eng. Chem.*, 2017, **47**, 41–45.
42 Q. Dong, H. Su, D. Zhang, W. Cao and N. Wang, *Langmuir*, 2007, **23**, 8108–8113.
43 J. Zhou, X. Wang, T. Ai, X. Cheng, H. Y. Guo, G. X. Teng and X. Y. Mao, *J. Dairy Sci.*, 2012, **95**, 4230–4236.
44 F. M. Sanakousar, C. C. Vidyasagar, D. B. Shikandar, N. Mounesh, C. C. Viswanatha and S. S. Chigari, *React. Chem. Eng.*, 2023, **9**, 388–409.
45 Z. A. Alrufaydi, S. M. Ahmed and A. T. Mubarak, *Mater. Res. Express*, 2020, **7**, 45103.
46 F. H. Ali Al-Jeboori, T. A. Mussa Al-Shimiesawi and O. M. Noori Jassim, *J. Chem. Pharm. Res.*, 2013, **5**, 172–176.
47 A. Ayub, A. Rauf, A. Anam, R. H. Alshammari, M. Z. Azam, N. Ambreen and M. Arshad, *RSC Adv.*, 2026, **16**, 13896–13913.
48 Z. F. Wu, Z. Wang, Y. Zhang, Y. L. Ma, C. Y. He, H. Li, L. Chen, Q. S. Huo, L. Wang and Z. Q. Li, *Sci. Rep.*, 2016, **6**, 22412.
49 M. Cheng, H. Fan, Y. Song, Y. Cui and R. Wang, *Dalton Trans.*, 2017, **46**, 9201–9209.
50 M. K. Kumawat, M. Thakur, J. R. Lakkakula, D. Divakaran and R. Srivastava, *Micron*, 2017, **95**, 1–6.
51 K. C. Das and S. S. Dhar, *Environ. Sci. Pollut. Res.*, 2020, **27**, 37977–37988.
52 H. Zhang, J. Wang and J. Yang, *Sci. Rep.*, 2020, **10**, 5545.
53 M. Esaifan, L. N. Warr, G. Grathoff, T. Meyer, M. T. Schafmeister, A. Kruth and H. Testrich, *Minerals*, 2019, **9**, 484.
54 R. Jacob, H. Hassan, A. Afify and G. Gabr, *Fresenius Environ. Bull.*, 2021, **30**, 8717–8727.
55 N. F. S. A. Kadir, N. M. Ahmad, S. A. S. Mohamad, L. S. Chua and E. T. T. Tan, *J. Teknol.*, 2022, **84**, 81–88.
56 O. U-Wang, R. B. Singh, W. B. Devi, U. I. Singh, R. B. Devi, O. B. Devi, R. Shahani and T. Swu, *Inorg. Nano-Met. Chem.*, 2019, **49**, 363–374.
57 B. Sharifa Zaithun, A. M. Emilia, T. Mohamed Ibrahim Mohamed, C. Karen Anne and A. R. Mohd Basyaruddin, *RSC Adv.*, 2018, **8**, 34004–34011.
58 R. M. Okasha, N. E. Al Shaikh, F. S. Aljohani, A. Naqvi and E. H. Ismail, *Int. J. Mol. Sci.*, 2019, **20**, 743.
59 J. Naseem, M. A. Rafea, M. E. A. Zaki, M. I. Attia, M. R. El-Aassar, F. Alresheedi, S. Zulfiqar and M. Aadil, *RSC Adv.*, 2025, **15**, 13940–13950.
60 H. Qu, H. Ma, W. Zhou and C. J. O'Connor, *Inorg. Chim. Acta*, 2012, **389**, 60–65.
61 X. Liu, M. Liang, M. Liu, R. Su, M. Wang, W. Qi and Z. He, *Nanoscale Res. Lett.*, 2016, **11**, 440.
62 M. Lin, L. Fan, Y. Qiu, Z. Li, Y. Wang, X. Cai, W. Li, F. R. Tay and X. Huang, *Acta Biomater.*, 2025, **203**, 604–621.
63 L. J. Bonales, V. Muñoz-Iglesias, O. Prieto-Ballesteros and E. Mateo-Martí, *Sci. Rep.*, 2022, **12**, 13677.
64 A. K. M. N. A. Siddiki, S. Islam, S. Begum and M. A. Salam, *Mater. Today: Proc.*, 2019, **46**, 6374–6381.
65 A. Mantion, L. Massüger, P. Rabu, C. Palivan, L. B. McCusker and A. Taubert, *J. Am. Chem. Soc.*, 2008, **130**, 2517–2526.
66 J. Cheng, C. Zhan, J. Wu, Z. Cui, J. Si, Q. Wang, X. Peng and L. S. Turng, *ACS Omega*, 2020, **5**, 5389–5400.
67 M. Khandelwal, K. Soni, K. P. Misra, A. Bagaria, D. S. Rathore, G. Pemawat, R. Singh and R. K. Khangarot, *RSC Adv.*, 2025, **15**, 3365–3377.
68 M. T. Uddin, M. Z. Bin Mukhlish and M. R. H. Patwary, *Desalin. Water Treat.*, 2021, **212**, 311–322.
69 F. Mubaraka, H. Rafique, J. Najeeb, S. Akram, H. Munir, S. Naeem, N. Kausar and N. Ashraf, *Int. J. Environ. Sci. Technol.*, 2024, **21**, 2489–2504.
70 W. M. Seleka and E. Makhado, *Int. J. Biol. Macromol.*, 2025, **305**, 141015.
71 R. Munir, D. Hamdani, Darnah, E. Marliana, R. Munir, S. H. Intifadhah and R. Kusuma, *MethodsX*, 2025, **14**, 103150.
72 Y. Li, J. Zhou, Y. Fan, Y. Ye and B. Tang, *Chem. Phys. Lett.*, 2017, **689**, 142–147.
73 C. D. Silvester and V. Raj, *ChemistrySelect*, 2025, **10**, e03225.
74 S. Liu, H. Lou, J. Luo, D. Albashir, Y. Shi and Q. Chen, *ACS Appl. Mater. Interfaces*, 2025, **17**, 19543–19561.
75 J. Zhang, W. Yuan, T. Xia, C. Ao, J. Zhao, B. Huang, Q. Wang, W. Zhang and C. Lu, *Nanomaterials*, 2021, **11**, 239.